Comparative Study of Ni- and Co-Substituted ZnO Nanoparticles: Synthesis, Optical, and Magnetic Properties

Imen Balti, Amine Mezni, Amel Dakhlaoui-Omrani, Philippe Leone, Bruno Viana, Ovidiu Brinza, Leila-Samia Smiri, Noureddine Jouini

Comparative Study of Ni- and Co-Substituted ZnO Nanoparticles: Synthesis, Optical, and Magnetic Properties

Imen Balti,[†,‡] Amine Mezni,[†] Amel Dakhlaoui-Omrani,[†] Philippe Léone,[§] Bruno Viana,[⊥] Ovidiu Brinza,[‡] Leila-Samia Smiri,[†] and Noureddine Jouini*[,‡]

[†]Unité de recherche 99/UR12-30, Faculté des Sciences de Bizerte, Université de Carthage, 7021 Jarzouna, Tunisia

[‡]Laboratoire des Sciences des Procédés et Matériaux, LSPM, CNRS, UPR 3407 Université Paris XIII, 99 Avenue J. B. Clément, 93430 Villetaneuse, France

[§]IMN—UMR/CNRS—Université de Nantes, 2 Chemin de la Houssière, 44 072 Nantes, France

[⊥]Ecole Nationale Supérieure de Chimie de Paris, 11 rue Pierre et Marie Curie, 75005 Paris, France

ABSTRACT: Ni- and Co-substituted ZnO nanoparticles were synthesized using forced hydrolysis of acetate metallic salts in a polyol medium. The X-ray diffraction patterns show a hexagonal wurtzite structure (space group $P6_3mc$). The character-istic absorption bands of UV-vis-IR spectra are correlated with the d-d transitions of tetrahedrally coordinated Co^{2+} and Ni^{2+} ions in octahedral and tetrahedral sites. The photoluminescence spectra exhibited a typical ZnO UV-exitonic emission band around 380 nm and a broad band between 400 and 500 nm that might be ascribed to the intrinsic defects in the ZnO material. The transmission electron microscopy displays spherical parti-cles with a diameter between 20 and 30 nm. The magnetic measurements reveal that Zn1-xNixO and Zn1-xCoxO nanoparticles show, respectively, ferromagnetic and paramagnetic behavior at 5 K. Homogeneous distributions of Co and Ni ions in the particles observed by filter imaging analysis indicates that there is no evidence of Co or Ni metal throughout the powders.

1. INTRODUCTION

Zinc oxide (ZnO) exhibits many interesting properties. It is an intrinsic n-type II—VI semiconductor with a direct dipole allowed band gap of 3.37 eV at room temperature and a large exciton binding energy of 60 meV. Because of these properties, ZnO presents a strong excitonic UV-light emission at room temperature. The emission intensity ratio between the near-band-edge (NBE) excitonic emission and the defect-related visible emission is classically used to evaluate the quality of ZnO crystals.[1−3] It also presents a high photoconductivity, and considerable piezoelectric and pyroeletric properties.[4,5] Because of these properties, ZnO has attracted much attention for potential applications in various electronic and optoelectronic devices. Moreover, the interest in ZnO has significantly been increased in the past decade after the publication of the primary results of Dietl et al. reporting ferromagnetism at room temperature (RT-FM) for diluted magnetic semiconducting (DMS) compounds,[6] such as 3d ions M^{2+}-substituted zinc oxide. This class of materials is potentially interesting for spintronic devices, such as spin valves, magnetic sensors, spin light-emitting diodes, and nonvolatile memory. However, intrinsic RT-FM in 3d transition substituted zinc oxide is still not proved and some results are contradictory.[7−13] For example, Pan et al.[14] reported the intrinsic existence of ferromagnetism in Co^{2+}:ZnO films. Contrarily, Djerdj et al.[10] explained the existence of ferromagnetic behavior as an extrinsic property of zinc oxide. Indeed, these researchers have shown that the solid solution $Zn_{1-x}Co_xO$ (x = 3 and 5 mol %) is ferromagnetic at room temperature due to the presence of cobalt clusters.

This paper reports on a comparative study of Ni- and Co-substituted zinc oxide nanoparticles obtained using forced hydrolysis in a polyol medium. Ni and cobalt have been selected in this work due to that (i) these two elements are stable with the valence +2 in a polyol medium and thus will substitute the zinc ion without generating significant cation site vacancy and that (ii) Co^{2+} can adopt more easily a tetrahedral site than Ni^{2+} does. This can induce a slightly different occupation of sites in the wurtzite structure, which, in turn, may induce different physical properties.

The synthesis method chosen here is a low-temperature process that allows higher doping levels of magnetic ions and leads to particles with high crystalline quality.[15] SQUID measurements reveal that the two materials present different magnetic behaviors. This difference will be discussed with regard to optical measurements and imaging filter analysis.

Table 1. Identified Phases as a Function of the Synthesis Conditions

sample	solvent	[Zn + M[a]]	% Ni	% Co	b[b]	h[c]	temperature (°C)	identified phases (XRD)
ZN_1	DEG	0.5	5		2	20	245	ZnO + lamellar phase
ZN_2	DEG	0.5	10		2	20	245	ZnO + lamellar phase
ZN_3	PEG	0.5	5		2	20	189	ZnO wurtzite
ZN_4	PEG	0.5	10		2	20	189	ZnO wurtzite
ZN_5	PEG	0.5	20		2	20	189	ZnO + lamellar phase
ZN_6	PEG	0.5	20		1	20	189	ZnO + lamellar phase
ZC_1	DEG	0.5		5	2	20	245	ZnO wurtzite
ZC_2	DEG	0.5		10	2	20	245	ZnO + lamellar phase
ZC_3	DEG	0.5		10	1	20	245	ZnO wurtzite
ZC_4	DEG	0.5		20	2	20	245	ZnO + lamellar phase
ZC_5	DEG	0.5		20	1	20	245	ZnO wurtzite
ZC_6	DEG	0.5		30	1	20	245	ZnO + lamellar phase
ZC_7	DEG	0.5		30	0.5	20	245	ZnO wurtzite
ZC_8	DEG	0.5		40	0.5	20	245	lamellar phase

[a] M = nickel or cobalt. [b] $b = n_{\text{sodium hydroxide}}/n_{\text{metal}}$. [c] $h = n_{\text{water}}/n_{\text{metal}}$.

2. EXPERIMENTAL PROCEDURE

2.1. Synthesis. Ni- and Co-substituted ZnO nanoparticles were prepared according to the following process. First, the appropriate amount (Table 1) of zinc acetate dihydrate ($Zn(Ac)_2 \cdot 2H_2O$), nickel acetate tetrahydrate ($Ni(Ac)_2 \cdot 4H_2O$) or cobalt acetate tetrahydrate ($Co(Ac)_2 \cdot 4H_2O$), sodium hydroxide (NaOH), and distilled water were successively introduced into 80 mL of polyol solvent (1,2-propanediol (PEG), diethylene glycol (DEG)), sonicated for 30 min. The total amount of metal (Zn and dopant metal M) was fixed at 0.5M. The pH of the solution varied in the range between 10 and 14 depending on the amount of sodium hydroxide (pH test paper). The as-obtained mixture was then heated under reflux to the boiling temperature of the solvent. After 6 h of reaction, the mixture was cooled to room temperature and the precipitate was separated from the supernatant by centrifugation (8000 rpm for 15 min), washed several times with ethanol and acetone, then dried in a vacuum at 50 °C. Several synthesis parameters, such as the temperature of the reaction, the nature of the solvent, the hydrolysis ratio ($h = n_{\text{water}}/n_{\text{metal}}$), and the basic ratio ($b = n_{\text{sodium hydroxide}}/n_{\text{metal}}$), were varied, and the most attractive results are summarized in Table 1.

2.2. Characterization. The chemical analysis of metal elements was conducted at the CNRS central analysis service at Solaize using inductively coupled plasma-atomic emission spectroscopy (ICP-AES).

X-ray diffraction (XRD) was performed on an INEL diffractometer using a cobalt Kα radiation (λ = 1.7890 Å). The data were collected for approximately 12 h.

Transmission electron microscopy (TEM) observations were made on a JEOL 2011 microscope operating at 100 kV. This microscope is equipped with a Gatan Imaging Filter 2000 so as to conduct an electron energy-loss spectroscopy (EELS) analysis. Such an analysis is a powerful technique to provide a cartographic picture of the distribution of chemical elements in the observed nanoparticles.

UV−visible-NIR diffuse reflectance spectra were recorded on a Cary 56^E spectrophotometer equipped with a PTFE-coated integration sphere.

The PL measurements were carried out at room temperature and at low temperature down to 20 K. The excitation source at 266 nm was provided by the YAG:Nd quadrupled frequency. The emission was analyzed by using a HR250 monochromator (Jobin-Yvon) coupled with an UV-enhanced intensified charge coupled device (ICCD, Roper). Under pulsed laser excitation, luminescence spectra were recorded in a pseudo CW mode with a continuous integration of the intensity during 300 ms corresponding to three full illumination pulses. The excitation power and the geometrical arrangement of the experiment were the same for the various investigated samples.

A superconducting quantum interference device (SQUID) magnetometer was used to measure the magnetic properties of Ni- and Co-doped zinc oxides. The hysteresis loops were recorded at 5 K. The thermal behavior of the magnetization was studied in the zero-field-cooled/field-cooled (ZFC/FC) modes at an applied magnetic field of 200 Oe.

Table 2. Nickel and Cobalt Concentration and Lattice Parameters for Substituted Zinc Oxide

	0% Ni	4.69% Ni	9.72% Ni		
a (Å)	3.249 (1)	3.241(1)	3.238(2)		
c (Å)	5.208 (2)	5.193(3)	5.186(2)		
	0% Co	4.88% Co	9.35% Co	18.35% Co	28% Co
a (Å)	3.249 (2)	3.247(1)	3.246(2)	3.243(1)	3.241(1)
c (Å)	5.208 (1)	5.206(3)	5.203(3)	5.199(3)	5.193(3)

3. RESULTS

3.1. X-ray Characterization. The exact composition of the as-obtained pure phases inferred from the chemical analyses is reported in Table 2. Nickel has a limited substitution concentration compared to cobalt, as previously reported for the solid solutions $Zn_{1-x}M_xO$ (M = Ni, Co).[16]

$ZnO:Ni^{2+}$ 0.05 < x < 0.20. In the case of $ZnO:Ni^{2+}$, the solubility appears to mainly depend on the nature of the polyol. On one hand, the powders $Zn_{(1-x)}Ni_xO$ (x = 0.5, 0.10) prepared in DEG at 245 °C with b = 2 and h = 20 (ZN_1 and ZN_2) consist of a mixture of ZnO wurtzite and a lamellar phase marked by asterisks (Figure 1A). The lamellar phase (d = 10.98 Å) can be

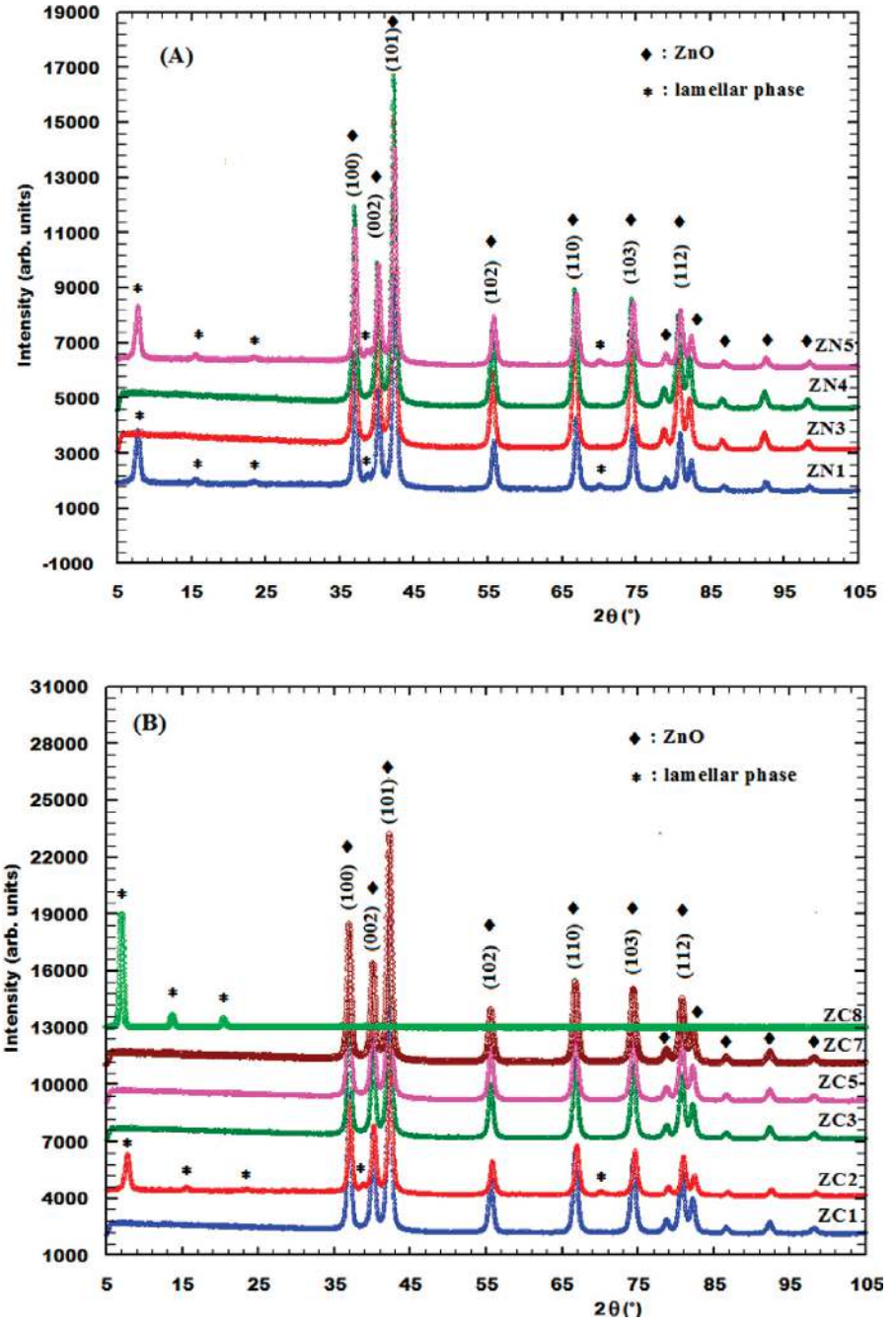

Figure 1. Powder X-ray diffraction patterns of samples according to compositions indicated in Table 1: (A) nickel-doped samples and (B) cobalt-doped ones. The square (♦) indicates zinc oxide with a wurtzite structure, and the asterisk (∗) indicates the lamellar hydroxy salt phase.

identified as the layered hydroxide salts LHS-Ni-Ac.[17] On the other hand, when the syntheses are conducted in PEG at 189 °C with $b = 2$ and $h = 20$ (ZN_3 and ZN_4), no peak corresponding to the lamellar phase is observed. Indeed, XRD patterns recorded for 12 h correspond perfectly to the zinc oxide wurtzite structure (space group $P6_3mc$, JCPDF 361451).

For compositions richer in nickel ($x > 0.10$), the powder is composed of a mixture of phases (ZnO wurtzite and a lamellar phase), whatever the basic ratio and the nature of the polyol.

$ZnO:Co^{2+}$ $0.05 < x < 0.40$. All tests were performed in DEG at 245 °C. The XRD patterns of the powders obtained are shown in Figure 1. The powder was obtained pure, ZC_1, in the same preparation conditions as ZnO ($b = 2$, $h = 20$). For a higher substitution rate, it was necessary to adjust the rate of basicity in order to obtain pure substituted ZnO oxide (ZC3: $b = 1$ for $x = 0.10$; ZC5: $x = 0.20$; and ZC7: $b = 0.5$ for $x = 0.30$). Otherwise, a lamellar phase (LHS) presenting an interlamellar distance of 12.15 Å (Figure 1B) appeared along with the substituted ZnO oxide: samples ZC_2, ZC_4, and ZC_6. When the substitution rate reached 40%, substituted ZnO oxide disappeared and only the LHS-Zn-Co is formed. These lamellar phases can be identified as the layered hydroxide salts based on zinc and cobalt.[17]

The lattice parameters were refined by the Rietveld method[18] from the XRD diffractogram (recorded for 12 h) using the

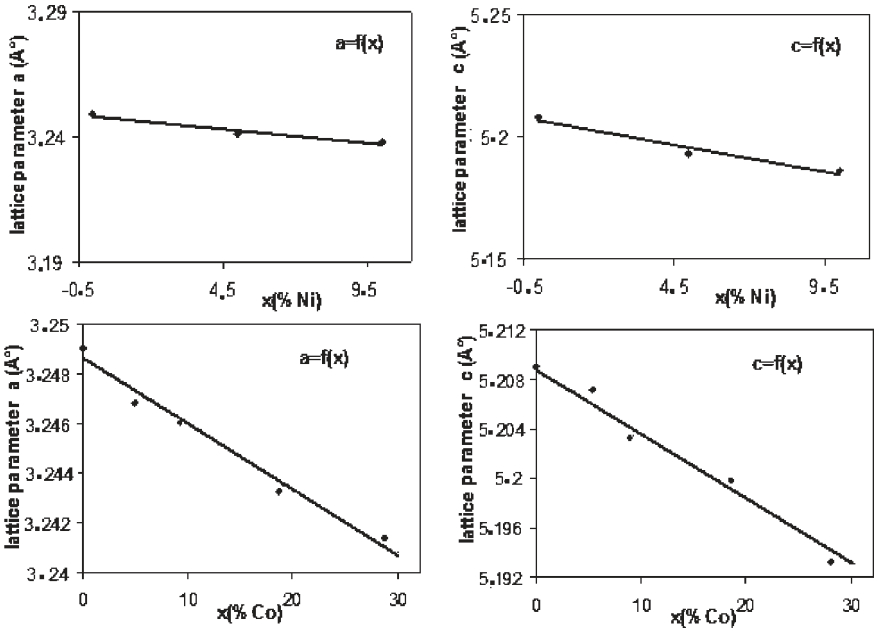

Figure 2. Variation of lattice parameters as a function of nickel and cobalt content in solid solutions $Zn_{1-x}Ni_xO$ (4.69% and 9.72%) and $Zn_{1-x}Co_xO$ (4.88, 9.35, 18.35, and 28%). The lattice parameters are slightly less than that of pure ZnO: the decreasing of *a* and *c* parameters are an indicator for Ni and Co substituting Zn in the ZnO crystalline structure.

program FULLPROF.[19] The values of lattice parameters of pure powders obtained for two series of syntheses are shown in Table 2.

The variation of lattice parameters *a* and *c* with the molar substitution of Zn^{2+}, *x*, is given in Figure 2. The lattice parameters decrease when the concentration of the dopant increases (Figure 2). Although the change is very small, the concentration of the dopant plays a role in the variation of lattice parameters that gives an indication for the Ni and Co substituting in the ZnO crystalline structure since the ionic radii of Ni^{2+} (0.055 nm) and Co^{2+} (0.058 nm) are less than that of Zn^{2+}(0.060 nm).[20]

3.2. Electron Microscopic Study. The TEM observations of samples ZN_3 (Figure 3A) and ZC_1 (Figure 3B) display almost spherical particles with a diameter between 20 and 30 nm. The distribution of elements in the powders is clarified by selecting and imaging the electrons with a specific energy loss. Analyses were driven on assemblies of particles (Figure 4) and also on isolated nanoparticles (Figure 5) at several regions of both Ni- and Co-doped ZnO samples. It reveals a homogeneous distribution of Ni (Figure $4A_2$) ions and Co (Figure $4B_2$) in the ZnO particles with no evidence of Ni or Co clusters. Concomitantly, imaging analysis shows that the distribution of Zn is also homogeneous for both cobalt- and nickel-substituted zinc oxides (Figure $4A_1$,B_2). A homogeneous composition inside of each nanoparticle is clearly observed in Figure 5.

3.3. UV−Visible-NIR Absorption. A plot of optical absorbance spectra of $Zn_{1-x}M_xO$ (M = Co, Ni) particles as a function of the wavelength is shown in Figure 6. Energies and assignments of the observed bands are given in Table 3 and compared to that of reference compounds with nickel[21,22] and cobalt.[15,23,24] It appears that Ni^{2+} and Co^{2+} present different d−d absorption bands. Indeed, Ni^{2+} is located in both octahedral and tetrahedral sites, whereas Co^{2+} is only located in tetrahedral sites. On the basis of the synthetic consideration of XRD and UV−vis−IR spectroscopy analysis results, it is clear that Co and Ni ions

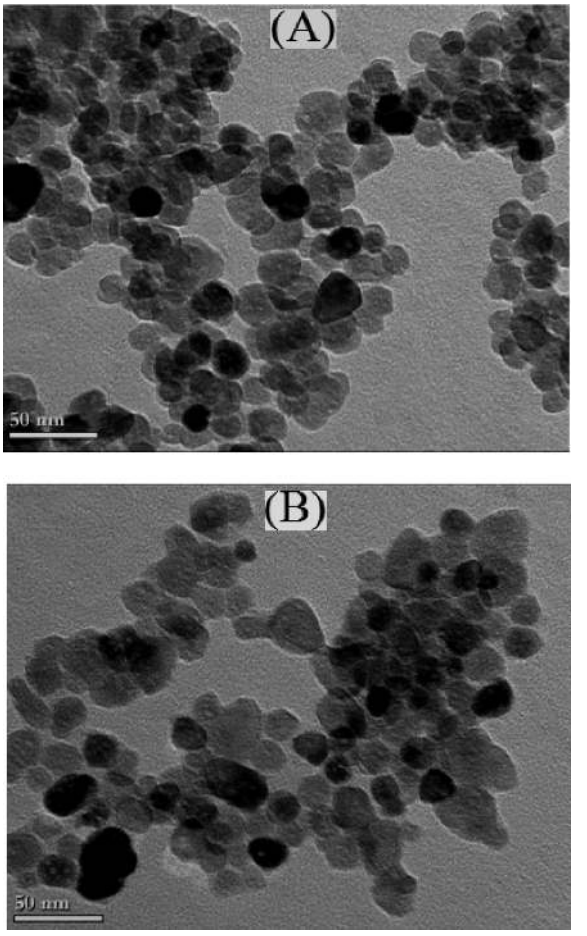

Figure 3. TEM images of (A) Ni (4.69%) and (B) Co (4.88%) substituted zinc oxide nanoparticles. The particles are roughly spherical, and the mean particle's size is about 20−30 nm.

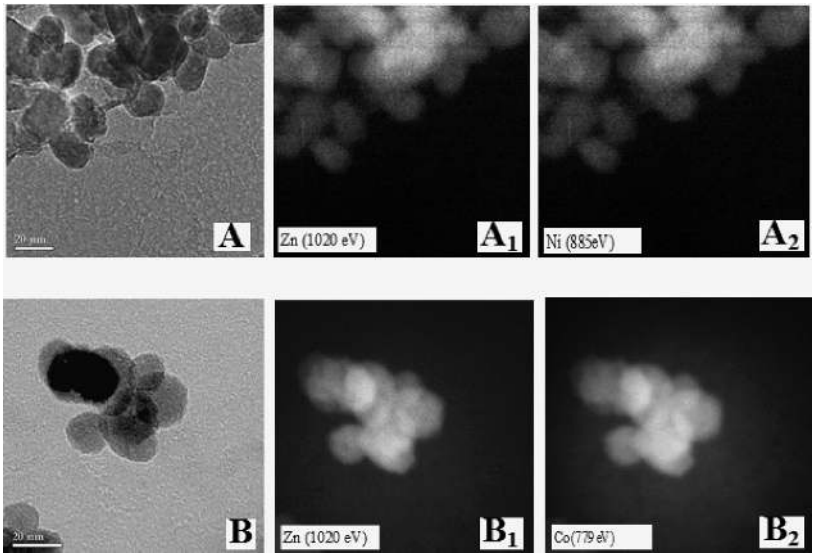

Figure 4. Filter imaging of (A) Ni (4.69%) and (B) Co (4.88%) substituted zinc oxide nanoparticles. It reveals a homogeneous distribution of Ni (A_2) and Co (B_2) in ZnO particles with no evidence of Ni or Co clusters. Concomitantly, filter imaging (A_1) and (B_1) show a homogeneous repartition of Zn.

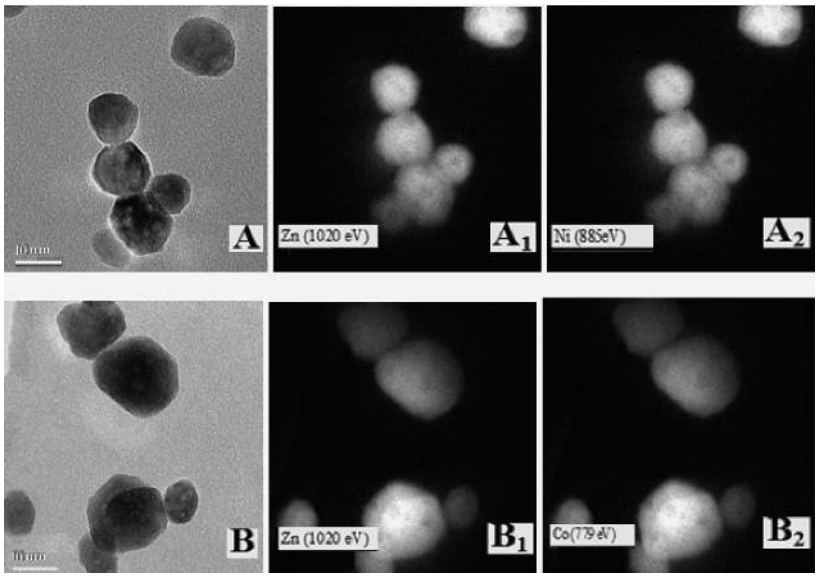

Figure 5. Filter imaging of (A) Ni (4.69%) and (B) Co (4.88%) substituted zinc oxide nanoparticles on isolated nanoparticles. As observed in agglomerated nanoparticles (Figure 4), these results confirm the homogeneous repartition of the chemical elements in both nickel- and cobalt-substituted zinc oxides.

substitute Zn ions within the employed Co and Ni range (4.88, 9.35, 18.35, and 28%) and (4.69% and 9.72%), respectively.

3.4. Photoluminescence. Figure 7 presents photoluminescence spectra of $Zn_{1-x}Ni_xO$ (Figure 7A) and $Zn_{1-x}Co_xO$ (Figure 7B) at different doping concentrations according to Table 2. All samples exhibited a typical ZnO UV-exitonic emission band around 380 nm. In addition to the excitonic UV emission, there exists a visible emission in the 2.2−2.9 eV range. Indeed, a broad band observed between 400 and 550 nm might be attributed to the intrinsic defects in the ZnO material. In the literature, such defects have been ascribed to various processes, such as oxygen vacancy (V_O), interstitial zinc (Zn_i), singly ionized oxygen vacancy ($V^{\bullet}_O$), antisite oxygen (O_{Zn}), zinc vacancy (V_{Zn}), and even oxygen interstitial (O_i).[25−28] The two series present, however, different photoluminescence spectra. Indeed, the VIS emission dominates in all the range of the studied temperature in the case of cobalt-doped zinc oxide. Conversely, in the case of nickel-doped zinc oxide, the VIS emission is very weak at room temperature and is enhanced when the temperature is decreased (Figure 7A, inset). Comparing the two series, it is clear that $Zn_{1-x}Ni_xO$ shows a very limited amount of defects. It is interesting to note that the visible band is often ascribed to defects near and beneath the surface.[29] Taking into account that both nickel- and cobalt-doped zinc oxide nanoparticles have a similar morphology and size, it can be concluded that the difference observed in PL measurements between cobalt zinc oxide and

nickel-doped zinc oxide could be related to the nature of the two Co^{2+} and Ni^{2+} cations rather than to the S/V ratio of the particle. Co^{2+} has a slightly lower ionic radius and also can easily be oxidized into Co^{3+}, in particular, when this cation is located near the particle surface. This will lead to a more deformed wurtize structure with considerable Zn site vacancies and/or inserted oxygen. On the contrary, the Ni^{2+} cation, being more stable, leads to limited defects. However, for this latter, because UV measurements presented before in this paper have shown that Ni^{2+} ions could occupy both tetrahedral and octahedral sites in keeping with recent reported results,[30] zinc vacancies could be present.

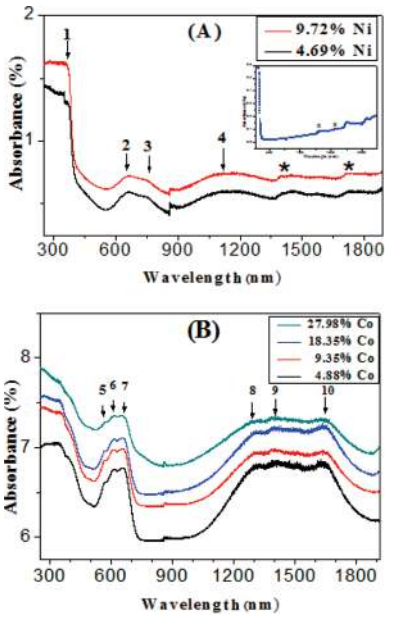

Figure 6. UV and near-IR absorption spectra of $Zn_{1-x}Ni_xO$ (A) and $Zn_{1-x}Co_xO$ (B) with different doping concentrations. The spectrum shows the expected electronic transitions for a Co^{2+} in tetrahedral coordination and Ni $^{2+}$ in both octahedral and tetrahedral sites. The bands marked with an asterisk are present in pure ZnO powder prepared in a polyol medium (inset).

At low temperature, excitonic emission vanishes in regard to the defect visible emission for both dopants, revealing energy transfers between the excitonic and defect states. In addition, both the UV emission and the defect-related peak intensity decrease in $Zn_{1-x}Ni_xO$ and $Zn_{1-x}Co_xO$ with the increase of Ni and Co doping concentrations. This probably could be attributed to nonradiative recombination processes[31] or to concentration quenching effects.[32]

3.5. Magnetic Measurements. The main results of magnetic measurements are summarized in Table 4.

ZnO:Ni^{2+}. The variation of the field dependence of magnetization at 5 K of 4.69% and 9.72% of Ni-substituted ZnO powder is shown in Figure 8. Hysteresis loops indicate the existence of ferromagnetic order. The coercitive fields measured are, respectively, 740 and 1143 Oe for the powder with 4.69% and 9.72% of Ni, in keeping with the previous results reported by Cong et al. on the $Zn_{0.97}Ni_{0.03}O$ sample.[33] The saturation magnetizations measured (0.583 and 0.599 emu·g^{-1} for 4.69% and 9.72% of Ni, respectively) are larger than that previously reported on Ni-doped ZnO nanoparticles.[34,35]

The curves of the thermal evolution of magnetic susceptibility are shown in Figure 9. The sudden increase in magnetic susceptibility and the change in slope observed on $\chi^{-1} = f(T)$ at 21 K for 4.69% can be attributed to the Curie temperature. The ferromagnetic behavior of these powders is probably due to superexchange interactions between Ni^{2+} ions.[36] The values of the Landé factor, around 2.2, are similar to those previously reported in several works.[17,37,38]

ZnO:Co^{2+}. The evolution curves of magnetization as a function of applied magnetic field at 5 K for two powders 4.88% and 9.35% of Co-substituted ZnO are given in Figure 10. The absence of hysteresis and the linear variation of the magnetic field dependence of the magnetization highlight the paramagnetic

Table 3. Bands Attribution of $Zn_{1-x}Ni_xO$ and $Zn_{1-x}Co_xO$ Powders UV−Visible-NIR Spectrum Compared to Tabulated Transitions for Some Cobalt- and Nickel-Based Reference Compounds

samples	wavelength	assignment	symmetry	ref
$Zn_{1-x}Ni_xO$	1196	ν_1: $^3A_{2g}(F) \rightarrow T_{2g}(F)$	Ni_{Oh}^{2+}, Ni_{Td}^{2+}	this work
	665	ν_2: $^3A_{2g}(F) \rightarrow {}^3T_{1g}(F)$		
	718	ν_{sf}: $^3A_{2g}(F) \rightarrow {}^1E_g(D)$	Ni_{Oh}^{2+}	
	380	ν_3: $^3A_{2g}(F) \rightarrow {}^3T_{1g}(P)$		
$Zn_{1-x}Co_xO$	568, 612, 650	ν_2: $^4A_2 \rightarrow {}^4T_1(F)$	Co_{Td}^{2+}	this work
	1309, 1406, 1645	ν_3: $^4A_2 \rightarrow {}^4T_1(P)$		
$ZnO:Ni^{2+}$	1192	ν_2: $^3A_2(F) \rightarrow {}^3T_1(F)$	Ni_{Td}^{2+}	22
	616, 656, 576	ν_3: $^3T_1(P) \rightarrow {}^3T_1(F)$		
β- $Ni(OH)_2$	1127	ν_1: $^3A_{2g}(F) \rightarrow T_{2g}(F)$	Ni_{Oh}^{2+}	21
	654	ν_2: $^3A_{2g}(F) \rightarrow {}^3T_{1g}(F)$		
	730	ν_{sf}: $^3A_{2g}(F) \rightarrow {}^1E_g(D)$		
	386	ν_3: $^3A_{2g}(F) \rightarrow {}^3T_{1g}(P)$		
$Zn_{0.75}Co_{0.25}O$	1628, 1388, 1310	ν_2: $^4A_2 \rightarrow {}^4T_1(F)$	Co_{Td}^{2+}	24
	660, 619, 570	ν_3: $^4A_2 \rightarrow {}^4T_1(P)$		
CoO	1200	ν_1: $^4T_{1g} \rightarrow {}^4T_{2g}(F)$	Co_{Oh}^{2+}	15
	606, 670	ν_2: $^4T_{1g} \rightarrow {}^4A_{2g}(F)$		
	550	ν_3: $^4T_{1g} \rightarrow {}^4T_{1g}(P)$		
Co_3O_4	720	ν_1: $^1A_{1g} \rightarrow {}^1T_{1g}$	Co_{Oh}^{3+}	23
	430	ν_2: $^1A_{1g} \rightarrow {}^1T_{2g}$		

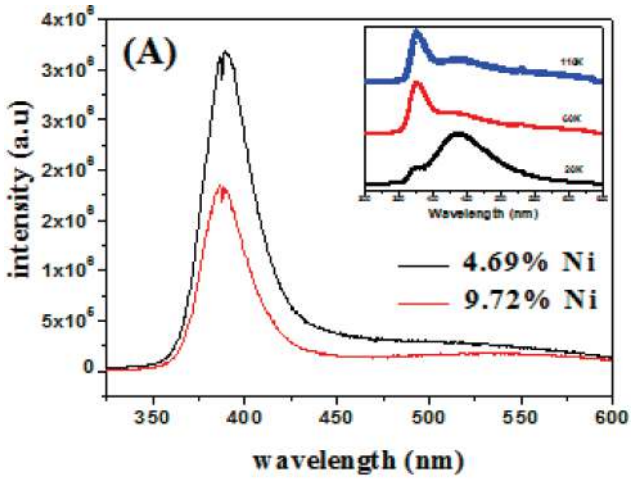

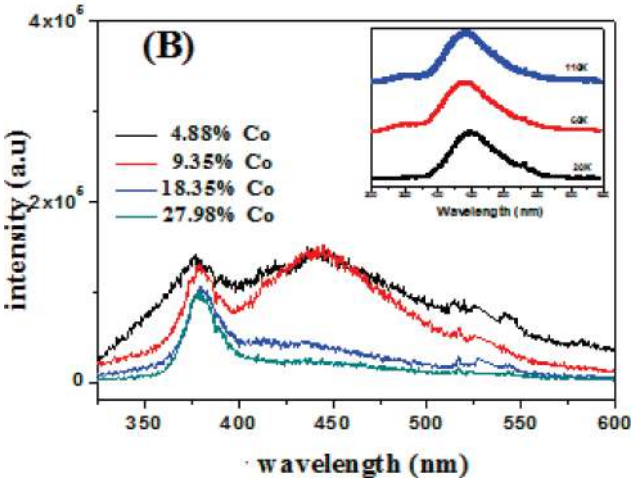

Figure 7. Photoluminescence spectra of $Zn_{1-x}Ni_xO$ (A) and $Zn_{1-x}Co_xO$ (B) nanoparticles at room temperature. Two main bands are observed: UV-excitonic emission band around 380 nm and a broad band observed between 400 and 550 nm ascribed to the intrinsic defects in ZnO. The insets show PL spectra at low temperatures (for $Zn_{1-x}Ni_xO$, x = 4.69%, and for $Zn_{1-x}Co_xO$, x = 4.88%) where the VIS emission band due to defects dominates.

Table 4. Magnetic Properties of Ni- and Co-Substituted Zinc Oxides

compounds	T_c/K	θ_p/K	H_c/Oe	$C/cm^3 \cdot mol^{-1} \cdot K$	g
4.69% Ni	21	23	740	1.22	2.21
9.72% Ni	22	25	1143	1.27	2.25
4.88% Co		17		2.72	2.75
9.35% Co		19		2.78	2.98

character of these compounds. We observed a similar behavior for the other compositions.

Measurements of the magnetic susceptibility of the sample $Zn_{1-x}Co_xO$ were performed in the temperature range of 5−300 K by applying a field of 200 Oe. Figure 11 shows the thermal evolution of the magnetic susceptibility χ and its inverse χ^{-1}. The variation of the reciprocal susceptibility χ^{-1} as a function of temperature follows the Curie−Weiss law ($\chi = C/T - \theta$). The linearity observed throughout the explored temperature range

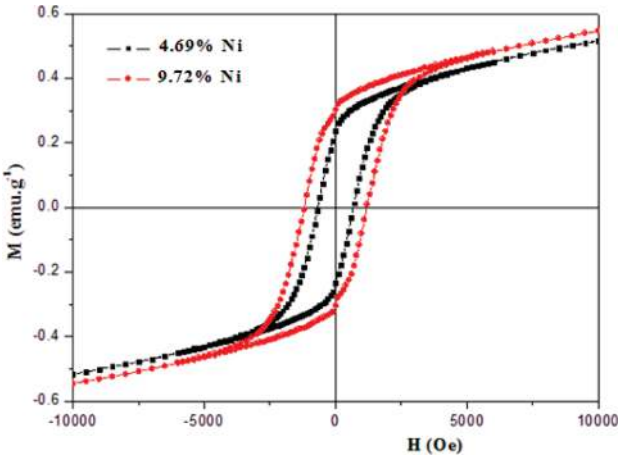

Figure 8. Magnetization (M) versus applied field (H) curve of $Zn_{1-x}Ni_xO$ samples measured at 5 K. The magnetic hysteresis loop is clearly observed, resulting from ferromagnetic character. The remanent magnetization (Mr) and coercive field (H_c) are 0.6 emu/g and 700−1200 Oe, respectively.

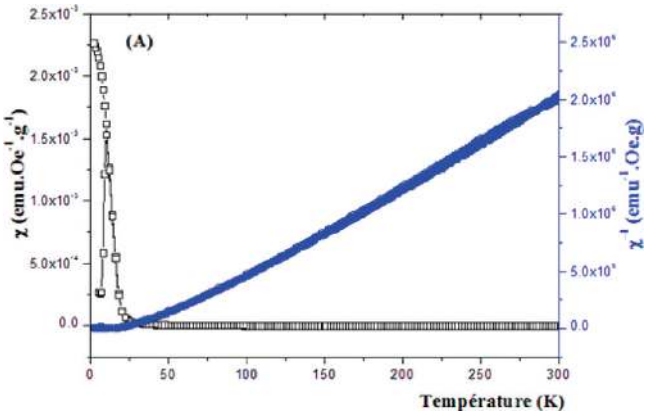

Figure 9. Temperature-dependent susceptibility χ and inverse susceptibility $1/\chi$ curves of 4.69% Ni-substituted zinc oxide nanoparticles at a magnetic field of 200 Oe. The abrupt increase in $\chi - T$ curves corresponds to a T_c of 21 K (the sample with 9.72% presents similar curves).

can assign to this powder a paramagnetic behavior. The absence of a maximum level of the curve $\chi = f(T)$ indicates the absence of a long-range magnetic order between the metal centers of spin 3/2 in the considered temperature range. The values of the Landé factor (2.78 and 2.98) are close to those previously reported.[39]

4. DISCUSSION

In two previous papers,[15,40] some of us reported on the synthesis of pure zinc and cobalt-doped zinc oxide in a polyol medium. The morphology and size of particles obtained depend on the experimental conditions. Spherical particles with a diameter in the micrometric or submicrometric range were obtained when (Zn, Co) salt precursors are heated in a polyol medium without adding sodium hydroxide. Adding sodium hydroxide induced significant changes in both morphology and size of the obtained particles in the case of pure zinc oxide. Indeed, varying the amount of hydroxide resulted in the obtention of zinc oxide nanoparticles with various morphologies: spherical, elliptical, and nanorod ones.[41] In the present paper,

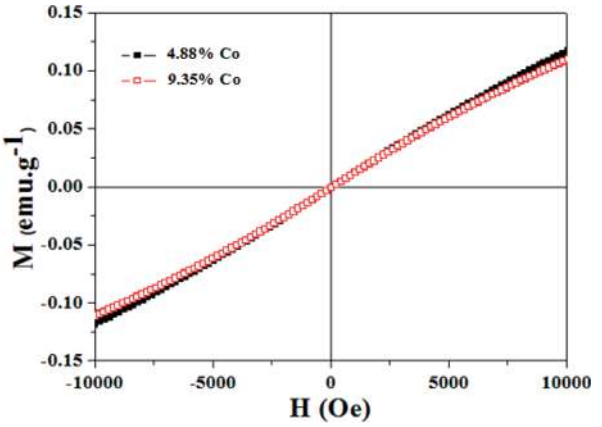

Figure 10. Magnetization curves at 5 K of cobalt-doped zinc oxides. The absence of hysteresis and the linear variation of the magnetization with magnetic field highlight the paramagnetic character of these compounds.

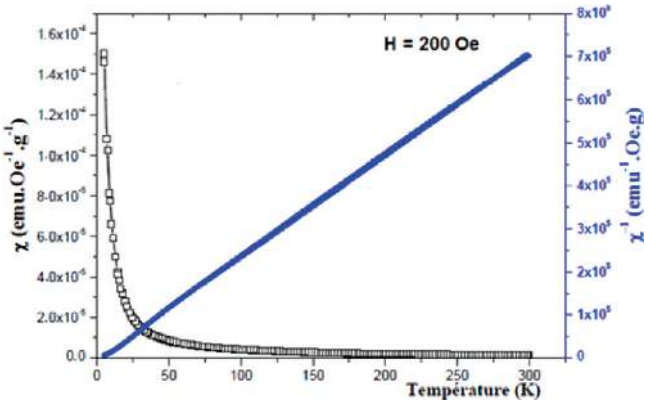

Figure 11. Susceptibility, χ, and inverse susceptibility, $1/\chi$, as a function of temperature of 4.88% Co-substituted zinc oxide (the sample with 9.35% presents similar curves).

we show that, when syntheses are conducted with sodium hydroxide in the polyol medium doped zinc oxide (Ni, Co), spherical nanoparticles can be obtained with 20−30 nm in diameter. Both doped zinc oxides obtained belong to the wurtzite-like structure. The cell parameters decreased when the amount of the doped element (Ni, Co) increased. This confirmed that the doped ions substituted Zn ions in the wurtzite structure since the ionic radius of these ions is lower than that of zinc. The imaging filter analysis supports this hypothesis. Indeed, the nanoparticles appeared to be homogeneous in composition. Despite these common features and the fact that all doped compounds were prepared under almost identical conditions, the cobalt-doped oxide has a paramagnetic behavior, whereas the nickel one presents a ferromagnetic character below 10 K.

Boubekri et al.[8] have studied the magnetic properties of micrometric cobalt zinc oxide particles prepared in a polyol medium. These micrometric particles are paramagnetic at room temperature. They became ferromagnetic when heated at high temperature due to the appearance of cobalt clusters. Such a conclusion has been inferred from indirect methods (electronic paramagnetic resonance for instance). In the present work, we have prepared particles with a significantly lower size lying in the range of 20−30 nm. Filter imaging analysis clearly shows that Co-doped zinc oxide prepared by soft chemistry is free of cobalt clusters. The UV spectrum is characteristic of Co^{2+} located in the tetrahedral sites, present in the wurtzite structure. One can note that the nanoparticles present a significant Zn and/or O defect, as evidenced by PL measurements. Such a defect, particularly oxygen vacancies, likely induces ferromagnetic behavior according to the donor impurity band exchange model.[42,43] Despite this high defect concentration, all the Co-doped nanoparticles present a paramagnetic behavior at room temperature similar to that reported by Boubekri et al. for Co-doped micrometric particles.

Conversely, Ni-doped zinc oxide nanoparticles with significantly lower defects present a ferromagnetic behavior below 10 K (coercitive field, 700−1000 Oe; saturation magnetization = 0.6 emu/g). A similar behavior has been reported by Cong et al. on the $Zn_{0.97}Ni_{0.03}O$ sample.[33] No nickel clusters are observed since the imaging filter analysis indicates a homogeneous spread of zinc and nickel on the overall nanoparticles. The presence the NiO phase can also be easily ruled out since bulk NiO is antiferromagnetic with a Neel temperature of 520 K.[44] As discussed above, Ni ions are present in both octahedral and tetrahedral coordination, similar to the nickel distribution in the inverse spinel $NiAl_2O_4$.[45] Because no secondary phase is revealed by X-ray diffraction, it can be deduced that Ni ions partly substitute the Zn ions in the tetrahedral sites and are partly intercalated in the vacant octahedral sites of the wurtzite structure. Such repartition may enhance the superexchange mechanisms leading to the observed ferromagnetic behavior. In this case, the ferromagnetism appears as an intrinsic character. It should, however, be noted that the presence of a ferromagnetic phase as an impurity, such as LHS-Ni,[17,43,46] in which Ni ions are located in the octahedral sites of the brucite-like structure, cannot be ruled out. Taking into account that no secondary phase was detected by X-ray diffraction, this means that the amount of LHS-Ni is lower than 5% (detection limit of X-ray analysis).

Finally, let us discuss the advantages offered by this method to obtain pure DMS compounds. A survey of the literature shows that several reported synthesis methods, such as magnetron sputtering,[43] solid-state reactions,[47,48] hydrothermal synthesis,[49] and spray pyrolysis,[50] involve several steps, including heat treatment at high temperature in an inert or reduced atmosphere. These thermal conditions favor the reduction of the metal ions to metal clusters, leading to a composite material formed mainly by doped zinc oxide decorated with metal clusters. These clusters appear to be the main species responsible for the ferromagnetism of the Co-doped zinc oxide. Thus, this ferromagnetism is an extrinsic character rather than an intrinsic one.

In the present work, we present an alternative route that obtains DMS nanoparticles free of metallic clusters. This synthesis method belongs to the sol−gel route and involves hydrolysis in a polyol medium. Because the formation of oxide occurred via nucleation, growth, hydrolyis, and inorganic polymerization processes,[51] the precipitation of reduced species, namely, metal (Co, Ni) clusters, can be avoided, and thus the magnetic properties of the as-obtained DMS compounds appeared to be closely related to intrinsic characteristics.

5. CONCLUSION

In summary, $Zn_{1-x}M_xO$ (M = Ni, Co) nanoparticles were synthesized by forced hydrolysis of acetate metallic salts in a polyol medium. The XRD patterns exhibit a single phase with a wurtzite structure. For a higher substitution amount ($x > 0.10$ for

M = Ni and $x > 0.30$ for M = Co), a secondary phase was observed. The effect of substitution of Zn^{2+} ions was investigated in Ni- and Co-doped ZnO in order to understand correlations between the structural, optical, and magnetic proprieties. Photoluminescence measurements demonstrated that both the UV emission and the defect-related emission peak intensity decreased in $Zn_{1-x}M_xO$ with increasing Co and Ni doping concentrations. Despite the fact that the two compounds were prepared by an almost identical soft chemistry method, they present different PL and magnetic behaviors. Although $Zn_{1-x}Co_xO$ has important defects, likely oxygen and zinc vacancies, this compound presents a paramagnetic character. Conversely, $Zn_{1-x}Ni_xO$ with very few defects shows a ferromagnetic character. Altogether, these results suggest that defects, mainly oxygen and zinc vacancies, in DMS compounds cannot be, as reported in the literature, the only driving force to promote ferromagnetism in such materials. Such ferromagnetism can be due to the presence of doped cations in both tetrahedral and octahedral sites of the wurtzite structure, as observed in the nickel-doped oxide. Indeed, such a presence may enhance an exchange mechanism favorable to ferromagnetic order.

Finally, we present in this work an alternative synthesis route to obtain DMS nanoparticles free of metallic clusters. This will be very useful with a view to preparing other pure DMS compounds and going further in the study of their potential magnetic properties.

AUTHOR INFORMATION

Corresponding Author

*E-mail: jouini@univ-paris13.fr. Tel: 33149403494. Fax: 33149403938.

ACKNOWLEDGMENT

This work was supported by "Institut français de cooperation en Tunisie". We would like to express our thanks to J-Y. Piquemal (ITODYS, Université Paris 7) for the UV−visible measurements, P. Aschehoug (Laboratoire de Chimie Appliquée de l'Etat Solide, École de Chimie à Paris) for the PL analysis, and J. Morrice-Abrioux (IUT Saint-Denis, Université Paris 13) for careful reading of the manuscript.

REFERENCES

(1) Ahn, C. H.; Kim, Y. Y.; Kim, D. C.; Mohanta, S. K.; Cho, H. K. *J. Appl. Phys.* **2009**, *105*, 013502.

(2) Chen, Y.; Bagnall, D. M.; Koh, H. J.; Park, K. T.; Hiraga, K.; Zhu, Z.; Yao, T. *J. Appl. Phys.* **1998**, *84*, 3912.

(3) Pauporte, T.; Jouanno, E.; Pelle, F.; Viana, B.; Aschehoug, P. *J. Phys. Chem. C* **2009**, *113*, 10422.

(4) Hsueh, T. J.; Hsu, C.-L. *Sens. Actuators, B* **2008**, *131*, 572.

(5) Rusu, G. G.; Girtan, M.; Rusu, M. *Superlattices Microstruct.* **2007**, *42*, 116.

(6) Dietl, T.; Ohno, H.; Matsukura, F.; Cibert, J.; Ferrand, D. *Science* **2000**, *287*, 1019.

(7) Belghazi, J. Y.; Schmerber, G.; Colis, S.; Rehspringer, J. L.; Berrada, A.; Dinia, A. *J. Magn. Magn. Mater.* **2007**, *310*, 2092.

(8) Boubekri, R.; Beji, Z.; Elkabous, K.; Herbst, F.; Viau, G.; Ammar, S.; Fiévet, F.; Von Bardeleben, H. J.; Mauger, A. *Chem. Mater.* **2009**, *21*, 843.

(9) Colis, S.; Bieber, H.; Bégin-Colin, S.; Schmerber, G.; Leuvrey, C.; Dinia, A. *Chem. Phys. Lett.* **2006**, *422*, 529.

(10) Djerdj, I.; Garnweitner, G.; Arcon, D.; Pregelj, M.; Jaglicic, Z.; Niederberger, M. *J. Mater. Chem.* **2008**, *18*, 5208.

(11) Jin, Z. W.; Fukumura, T.; Kawasaki, M.; Ando, K.; Saito, H.; Sekiguchi, T.; Yoo, Y. Z.; Murakami, M.; Matsumoto, Y.; Hasegawa, T.; Koinuma, H. *Appl. Phys. Lett.* **2001**, *78*, 3824.

(12) Pandey, B.; Ghosh, S.; Srivastava, P.; Avasthi, D. K.; Kabiraj, D.; Pivin, J. C. *J. Magn. Magn. Mater.* **2008**, *320*, 3347.

(13) Thota, S.; Kukreja, L. M.; Kumar, J. *Thin Solid Films* **2008**, *517*, 750.

(14) Song, C.; Zeng, F.; Geng, K. W.; Wang, X. B.; Shen, Y. X.; Pan, F. *J. Magn. Magn. Mater.* **2007**, *309*, 25.

(15) Poul, L.; Ammar, S.; Jouini, N.; Fiévet, F.; Villain, F. *Solid State Sci.* **2001**, *3*, 31.

(16) Bates, C. H.; White, W. B.; Roy, R. *J. Inorg. Nucl. Chem.* **1966**, *28*, 397.

(17) Taibi, M.; Ammar, S.; Jouini, N.; Fièvet, F.; Molinié, P.; Drillon, M. *J. Mater. Chem.* **2002**, *12*, 3238.

(18) Rietveld, H. M. *J. Appl. Crystallogr.* **1967**, *22*, 151.

(19) Rodriguez, C. J. *Collected Abstract of Powder Diffraction Meeting*. Toulouse, France, 1990, 127.

(20) Shannon, R. D. *Acta Crystallogr., Sect. A* **1976**, *32*, 751.

(21) Davidson, A.; Tempere, J. F.; Che, M.; roulet, H.; Dufour, G. *J. Phys. Chem.* **1996**, *100*, 4919.

(22) Papalardo, R. *J. Chem. Phys.* **1961**, *82*, 473.

(23) Brick, Y.; Kacimi, M.; Ziyad, M.; Bozon-Verduraz, F. *J. Catal.* **2001**, *202*, 118.

(24) Cossee, P.; Van Arkel, A. E. *J. Phys. Chem. Solids* **1960**, *15*, 1.

(25) Bylander, E. G. *J. Appl. Phys.* **1978**, *49*, 1188.

(26) Lin, B.; Fu, Z.; Jia, Y. *Appl. Phys. Lett.* **2001**, *79*, 943.

(27) Ozgur, U.; Alivov, Y. I.; Liu, C.; Teke, A.; Reshchikov, M. A.; Dogan, M. A.; Avrutin, V.; Cho, S. J.; Morkoc, H. *J. Appl. Phys.* **2005**, *98*, 041301.

(28) Vanhauheusden, K.; Warren, W. L.; Seager, C. H.; Talland, D. R.; Voigt, J. A.; Gnade, B. E. *J. Appl. Phys.* **1996**, *79*, 7983.

(29) Tay, Y. Y.; Tan, T. T.; Li, S. *Solid State Commun.* **2011**, *151*, 372.

(30) Elilarassi, R.; Chandrasekaran, G. *Mater. Chem. Phys.* **2010**, *123*, 450.

(31) Cheng, C.; Xu, G.; Zhang, H.; Luo, Y.; Li, Y. *Mater. Lett.* **2008**, *66*, 3733.

(32) Hong, R. J. *J. Cryst. Growth* **2011**, *314*, 30.

(33) Cong, C. J.; Hong, J. H.; Liu, Q. Y.; Liao, L.; Zhang, K. L. *Solid State Commun.* **2006**, *138*, 511.

(34) Lia, B. B.; Xiua, X. Q.; Zhanga, R.; Taoa, Z. K.; Chena, L.; Xie, Z. L.; Zheng, Y. D. *Mater. Sci. Semicond. Process.* **2006**, *9*, 141.

(35) Wu, D.; Yang, M.; Huang, Z.; Yin, G.; Liao, X.; Kang, Y.; Chen, X.; Wang, H. *J. Colloid Interface Sci.* **2009**, *330*, 380.

(36) Goodenough, J. B. *Magnetism and the Chemical Bond*. J. Wiley and Sons: New York, 1963.

(37) Hornick, C.; Rabu, P.; Drillon, M. *Polyhedron* **2000**, *19*, 259.

(38) Vilminot, S.; Richard-Plouet, M.; Andre, G.; Swierczynski, D.; Bourée-Vigneron, F.; Kurmoo, M. *Inorg. Chem.* **2003**, *42*, 21.

(39) Livage, C.; Egger, C.; Frey, G. *Chem. Mater.* **1999**, *11*, 1546.

(40) Jézéquel, D.; Guenot, J.; Jouini, N.; Fièvet, F. *J. Mater. Res.* **1995**, *10*, 77.

(41) Dakhlaoui, A.; Jendoubi, M.; Smiri, L. S.; Kanaev, A.; Jouini, N. *J. Cryst. Growth* **2009**, *311*, 3989.

(42) Coey, J. M. D.; Venkatesan, M.; Fitzgerald, C. B. *Nat. Mater.* **2005**, *4*, 173.

(43) Hou, D. L.; Zhao, R. B.; Wei, Y. Y.; Zhen, C. M.; Pan, C. F.; Tang, G. D. *Curr. Appl. Phys.* **2010**, *10*, 124.

(44) Schwartz, D. A.; Kittilstved, K. R.; Gamelin, D. R. *Appl. Phys. Lett.* **2004**, *85*, 1395.

(45) Jitianu, M.; Jitianu, A.; Zaharescu, M.; Crisan, D.; Marchidan, R. *Vib. Spectrosc.* **2000**, *22*, 75.

(46) Poul, L.; Jouini, N.; Fiévet, F. *Chem. Mater.* **2000**, *12*, 3123.

(47) Mao, X.; Zhong, W.; Du, Y. *J. Magn. Magn. Mater.* **2008**, *320*, 1102.

(48) Risbud, A. S.; Spaldin, N. A.; Chen, Z. Q.; Stemmer, S.; Seshadri, R. *Phys. Rev.* **2003**, *B 68*, 205.

(49) Cheng, C.; Xu, G.; Zhang, H.; Luo, Y.; Li, Y. *Mater. Lett.* **2008**, *62*, 1617.

(50) Subramanian, M.; Tanemura, M.; Hihara, T.; Ganesan, V.; Soga, T.; Jimbo, T. *Chem. Phys. Lett.* **2010**, *487*, 97.

(51) Poul, L.; Ammar, S.; Jouini, N.; Fievet, F. *J. Sol-Gel Sci. Technol.* **2003**, *26*, 261.